Label-free intraoperative histology of bone tissue via deep-learning-assisted ultraviolet photoacoustic microscopy

Rui Cao[1], **Scott D. Nelson**[2], **Samuel Davis**[1], **Yu Liang**[4], **Yilin Luo**[1], **Yide Zhang**[1], **Brooke Crawford**[3,*], **Lihong V. Wang**[1,*]

[1]Caltech Optical Imaging Laboratory, Andrew and Peggy Cherng Department of Medical Engineering, Department of Electrical Engineering, California Institute of Technology, Pasadena, CA 91125, USA

[2]Department of Pathology, David Geffen School of Medicine at UCLA, Los Angeles, CA 90095, USA

[3]Department of Orthopedic Surgery, David Geffen School of Medicine at UCLA, Los Angeles, CA 90095, USA

[4]Department of Pathology, City of Hope, Duarte, CA 91010, USA

Abstract

The rapid histopathological examination of bone tissue remains a challenge for orthopaedic oncologists due to the difficulty in performing cryosection-based analyses of bone tissue. Orthopaedic oncologists instead rely on pre-operative x-ray computed tomography or magnetic resonance imaging to identify the bony edge for a resection, a workflow which does not allow an accurate diagnosis or the confirmation of negative tumour margins in the resected tissue, leading to bone margin delimitation which can be up to 10-times wider than necessary in bony sarcomas (typically 2 cm from the tumour). Here, we report that 3-dimensional contour-scan reflection-mode ultraviolet (UV) photoacoustic microscopy (PAM) provides a label-free approach for the evaluation of unprocessed thick human bone specimens. The UV-PAM images of both undecalcified and decalcified bone specimens were validated with gold-standard hematoxylin and eosin stained images. An unsupervised deep learning algorithm based on cycle-consistent generative adversarial networks converted the UV-PAM images into H&E-like pseudocolor histologic images, allowing the pathologists to readily identify the cancerous features following existing pattern-recognition parameters.

Approximately 18.1 million new cancer cases were diagnosed worldwide in 2018, while the number of new cancer cases per year is expected to rise to 29.5 million, with 9.6 million cancer-related deaths by 2040[1]. Despite the advances in cancer treatment, surgery remains the cornerstone, and more than 80% of cancer patients have a surgical procedure at some point in the cancer evolution[2,3]. In oncologic surgery, intraoperative pathological examination provides surgical guidance and identification of tumor margins[4]. The border of the removed tissue in tumor surgery is often examined by intraoperative frozen section to ensure negative margins, meaning normal tissue surrounding the resected tumor[5]. Most localized tumors with negative margin resection show much better outcomes and a lower chance of tumor recurrence. The intraoperative evaluation of tumor margins allows confirmation of complete tumor resection before oncologic surgeons close the surgical wound and helps patients avoid the second tumor resection surgery.

To provide rapid pathological examination and guide tumor resection, oncologic surgeons currently rely on the frozen section technique, which typically takes a small portion of tissue and freezes the tissue in a cryostat machine[6]. The frozen tissue is then cut into thin sections (5-8 μm) using a microtome or cryostat and stained for direct examination under a microscope. However, the need for sectioning the specimen into thin slices prevents this technique from being used for hard tissue and may also cause inevitable tissue loss. For instance, the rapid pathological examination of calcified bone (cortical bone and calcified tumors) often cannot be evaluated by the frozen section technique due to the ossification[7,8]. It is usually impossible to directly cut the undecalcified bone tissue into slices thin enough for traditional pathological examination. Instead, the bone must undergo a decalcification process that can take up to several days, which may introduce artifacts if under-decalcified or over-decalcified[9].

The difficulties of rapid pathological examination of bone specimens have been a long-standing challenge for orthopedic oncologists in medical practice. For orthopedic oncologists resecting primary bone tumors, the need for time-consuming decalcification procedures often obviates pathological analysis during the operation. Thus, the surgeons tend toward wider margins based on pre-surgical imaging of bone tumors rather than intraoperative tissue analysis. Although wider margins are desirable for local tumor control, the functional loss can be much greater if those margins include vital structures such as tendons, nerves, blood vessels, or joints. Many surgeons use 2 centimeters as the ideal bony margin and measure this off the pre-operative imaging, while a meta-analysis performed in 2019 showed that a 2 millimeter margin is sufficient to avoid local recurrence[10]. Since calcified primary bone tumors, such as osteosarcoma, present most commonly in a periarticular location, 1.8 centimeters of margin difference could lead to joint salvage, increased patient bone stock for any future surgery needed, and less morbidity[10]. A modality that allows for fast, accurate bony margin analysis would be an invaluable tool in limb-salvage surgery.

In recent years, rapid developments of imaging techniques have revolutionized many biological and biomedical areas as well as pathology. Multiple fluorescence microscopy methods have been demonstrated for diagnostic imaging, including confocal microscopy[11], wide-field structured-illumination microscopy (SIM)[12,13], light-sheet microscopy[14], and

microscopy with UV surface excitation (MUSE)[15]. However, these fluorescence microscopy techniques require dye staining of the specimen to provide image contrast, which involves complicated and different procedures for various samples prior to imaging and needs highly experienced personnel. Label-free optical imaging techniques have also been developed for rapid pathological diagnoses, such as stimulated Raman scattering microscopy (SRS)[16,17] and coherence tomography/microscopy (OCT/OCM)[18,19]. However, although MUSE and SRS techniques provide fast surface imaging of slide-free specimens, they lack the depth-resolving capability and suffer from the limited depth of field, resulting in blurred images of uneven surfaces with unprocessed slide-free specimens. The deconvolution-based image fusion and multi-layer z stacked images can be used to achieve an extended depth of field. But it usually takes much longer imaging time and requires careful camera calibration and tedious experimental measurement of the point spread function, which are highly sensitive to noise or image variability[20]. While OCT has the depth-resolving capability, it cannot provide direct nuclear contrast within tissues since the optical scattering contrast does not have sufficient chromophore specificity[21]. Thus, OCT images cannot well match the current pathology standard of hematoxylin and eosin (H&E) staining in detail, which limits its application as a pathological diagnostic tool. The comparison between different imaging modalities and traditional pathology approaches can be found in Supplementary Table 1.

Flatness is difficult to achieve in calcified bone tumors resected during operation, as cutting hard and calcified bone inevitably leads to rough surfaces. To address these challenges, we have developed the real-time 3D contour-scan ultraviolet photoacoustic microscopy (UV-PAM) and demonstrated the label-free imaging of thick unprocessed bone, which requires minimal tissue preparation. The capability of imaging the non-sectioned bone specimen allows direct visualization of well-preserved structure and composition of calcifications, which could make UV-PAM potentially an ideal tool for rapid diagnosis of challenging tissues like thick calcified bone specimens. As a hybrid imaging modality, photoacoustic tomography (PAT) detects either endogenous or exogenous contrast-induced ultrasound signals through light absorption[22,23]. The wavelength-dependent absorption allows PAT to quantitatively measure the concentration and distribution of different optical absorbers, while the less scattering ultrasound detection enables high-resolution deep tissue imaging. The unique advantage of scalable spatial resolutions and imaging depths makes PAT attractive for various applications, ranging from imaging of nanometer-scale mitochondria to millimeter-level blood vessels in deep tissue[22]. Based on the imaging resolution and reconstruction approaches, PAT can be implemented in the form of either photoacoustic computed tomography (PACT) or photoacoustic microscopy (PAM)[23]. While PACT is mostly used for deep tissue imaging at the ultrasound resolution, PAM is often implemented with the optical diffraction-limited resolution. Utilizing the nonlinear absorption or Grüneisen parameter, PAM is also capable of achieving super-resolution imaging beyond the optical diffraction limits[24-26]. Depending on the illumination wavelength, various contrasts have been imaged by label-free PAM, including but not limited to hemoglobin[27,28], DNA/RNA[29], cytochrome[30], water[31], lipid[32], and protein[33].

In this study, we developed the UV-PAM system using a 266 nm nanosecond pulsed laser and demonstrated histology-like imaging of bone specimens. We implemented a real-time 3D contour-scanning mechanism to ensure consistent and optical diffraction-limited

resolution for uneven bone specimen surfaces, which does not need prior knowledge of the surface profile. Using the UV-PAM system, we demonstrated the histology-like imaging of unprocessed thick bone specimens with rough surfaces, which is challenging for traditional histological techniques. The UV-PAM images of both decalcified and undecalcified bone sections were acquired and compared with gold-standard H&E-stained images for validation. In addition, we present an unsupervised deep learning-based method to perform virtual H&E staining of grayscale UV-PAM images to provide the pathologist with complementary contrast and help interpret PAM images. Unlike supervised deep learning methods such as generational adversarial networks (GAN)[34,35], our unsupervised deep learning method based on cycle-consistent generational adversarial networks (CycleGAN) does not require coupled pairs of stained and unstained images[36,37]. It avoids the need for well-aligned UV-PAM and H&E-stained images for neural network training, which can be challenging to acquire due to artifacts caused by sample preparation-induced morphology changes. All experiments and protocols in this study are approved by the Institutional Review Boards at the California Institute of Technology, the University of California at Los Angeles, and the City of Hope.

Results

Histopathological examination of bone tissue via UV-PAM.

With optical focusing and the time-of-flight information from photoacoustic (PA) signals, PAM images the contrast distribution in 3D. The PA signal was received by a 42 MHz ultrasound transducer and digitized by a data acquisition card sampling at 500 MHz. We found that PAM can localize the z positions of the sample surface with accuracy finer than the acoustical resolution (~40 μm) by approximately a factor of 10 as limited by the signal-to-noise ratio. The UV-PAM employs a 266 nm nanosecond pulsed laser to image the DNA/RNA. While the penetration depth depends on the sample type, in bone specimens, we found that the UV light penetration is less than the acoustical resolution. Thus, no deep PA signal is generated and mixed with surface signals, allowing direct imaging of the surfaces of thick bone specimens. While soft tissue can be sampled or squeezed with a flat surface, unprocessed hard tissues (i.e., calcified primary bone, Supplementary Fig. 1) usually have a rough surface due to tissue extraction.

The 3D contour-scanning UV-PAM (Fig. 1a) allows direct imaging of thick specimens with rough surfaces, provides the possibility of rapid pathological diagnosis of undecalcified thick bone. Since the height differences in adjacent B-scan positions (0.625 μm away from each other) can be reasonably assumed to be much smaller than the depth of focus (DOF) of our UV-PAM (~9 μm), the z contour-scanning trajectory can be predicted and updated in real-time after the first seed B-scan for the full field of view (FOV), without the prior knowledge of the surface contour (Supplementary Fig. 2). Thus, the real-time 3D contour scanning UV-PAM can ensure the distance between the image position and focal plane is within the DOF, resulting in a consistent diffraction-limited lateral resolution for rough surface imaging. The performance of the proposed contour scanning mechanism has been tested using a phantom with a bent black tape, which showed well-compensated distances

in the full FOV (Supplementary Fig. 3a-c). The measured lateral resolution is 0.96 μm (Supplementary Fig. 3d).

After acquiring a grayscale UV-PAM image of the sample surface, the unsupervised deep learning method based on CycleGAN is used to implement the virtual staining. The deep learning network architecture (Fig. 1b) for virtual staining consists of two generators (G and F) and corresponding adversarial discriminators (D_{PA} and D_{HE}). Each pair of generators and discriminators are trained so that the outputs of G and F are indistinguishable from real PAM and H&E-stained images, respectively. The generators are further regularized using the cycle-consistency loss – transforming an image from one domain and back should recover the original input. This process ensures that the transformations are bijective and produce corresponding morphology. The combination of cycle consistency and discriminator loss terms avoids the necessity for well-aligned paired datasets, which are needed in traditional l_2-norm or similar loss training between a network output and a target label. With the neural network well trained, it takes less than 5 seconds to virtually stain an image of 1600×1600 pixels.

Thanks to the real-time 3D contour-scanning UV-PAM system and deep learning-assisted virtual staining, the rapid diagnosis of unprocessed bone becomes possible. The workflows of both PA histology and traditional H&E histology of bone clearly reveal the advantage of PA histology (Fig. 1c). While the frozen section technique is not applicable to hard bone specimens, conventional H&E histology techniques for bone can take up to 7 days. In contrast, the PA histology technique can produce virtually stained images of unprocessed bone for pathological examination within 11 minutes (0.625 μm step size, 1×1 mm² FOV).

3D contour-scanning UV-PAM of thick patient bones.

To demonstrate the imaging of unprocessed thick bone specimens for rapid pathological diagnosis, we extracted mineralized primary bone specimens from patients in a tumor resection surgery. Unprocessed bone specimens were immediately fixed in the formalin solution after surgical excision to prevent degradation. No further cutting or sectioning was implemented with the bone specimen, avoiding the need for paraffin or agarose embedding. Then, the bone specimen was placed onto a customized water-immersed sample holder for scanning. We obtained the left tibia bone specimens from a patient with osteofibrous dysplasia-like adamantinoma, which has a rough surface due to the surgical excision by an oscillating saw. The image acquired by 2D raster scanning without contour compensation (Fig. 2a) shows a large portion of the out-of-focus area within the FOV (2.5×6.25 mm²), resulting in an inconsistent resolution and poor image quality. The rough bone surface profile is reconstructed by the PA signal time-of-flight information (Fig. 2b), revealing a large fluctuation in surface height and less than 10% of the pixels within the DOF. In contrast, the UV-PAM image acquired by the 3D contour scanning of the same area showed significantly improved image quality and consistent resolution across the FOV (Fig. 2c). More than 92% of the surface area is within the small DOF during the 3D contour scanning (Fig. 2d). Another comparison between the 2D raster-scanning PAM image and the 3D contour-scanning PAM image of unprocessed patient bone can be found in Fig. 2e and Fig. 2f. As shown in Fig. 2f, important bone structures, such as trabeculae and marrow, can

be visualized by UV-PAM with specimen integrity. More 3D contour-scanning UV-PAM demonstrations of undecalcified thick bone specimens can be found in Supplementary Fig. 4 and Supplementary Fig. 5. It clearly shows that the 3D contour-scanning UV-PAM system is capable of imaging the rough surfaces of unprocessed thick bone specimens. In contrast, it is difficult to acquire high-quality images using the traditional 2D raster-scanning approach. Since UV-PAM imaging is non-destructive, the unprocessed bone specimens can be used for further pathological diagnosis.

H&E validation for label-free UV-PAM of bone specimens.

Since the traditional H&E-stained slice of bone usually requires decalcification and cutting into thin sections (i.e., 5-8 μm), we first demonstrated UV-PAM imaging of a formalin-fixed paraffin-embedded (FFPE) decalcified bone fragment without malignancy on a glass slide. As shown in Figs. 3a and 3c, obvious bone structures, including decalcified mineralized bone, can be readily visualized. In addition, the close-up images (Figs. 3b and 3d) demonstrate profiles and nests of metastatic carcinoma within the medullary space of the bone. The decalcified bone specimen from the patient with chondroblastic osteosarcoma is also imaged by UV-PAM and shown in Supplementary Fig. 6.

To validate the PA histology of bone fragments, we compared UV-PAM images of both decalcified and undecalcified bone specimens with gold-standard H&E-stained images acquired by a traditional optical microscope. Here, the contrast of PAM images is reversed to highlight the high absorption region in dark color for better comparison with H&E-stained images. A comparison between the original grayscale image and the image in reversed contrast can be found in Supplementary Fig. 7. The decalcified bone section on a glass slide extracted from a patient with metastatic adenocarcinoma was imaged by UV-PAM (Fig. 4a) and compared with its corresponding H&E-stained image (Fig. 4c). The UV-PAM image demonstrates the key features present in the H&E-stained image, in which abnormal tumor glands are readily observable (indicated by arrows). Meanwhile, the PAM image of a decalcified fragments of bone and hematopoietic marrow with no evidence of metastatic carcinoma (Fig. 4b) also shows the same structure as its corresponding H&E result (Fig. 4d). Furthermore, the undecalcified bone slices were imaged by PAM and compared with H&E-stained images, which avoids potential artifacts introduced by the decalcification procedures. Since these specimens were harvested from a portion of the tumor with low calcification, they did not require the decalcification procedure to section the specimen into thin slices. The PAM images (Fig. 5a-c) of undecalcified bone sections on a glass slide are presented in reverse contrast. Fig. 5a and Fig. 5b demonstrate features of osteoblastic osteosarcoma, while Fig. 5c demonstrates the myxoid lobules of chordoma. The corresponding H&E-stained images are acquired by the digital whole slide scanning microscope with a 40X objective (Fig. 5d-f)., showing essentially identical structures as the PAM images. Close-up images in sliding windows are shown in Supplementary Movie 1. Another example of UV-PAM and H&E comparison can be found in Supplementary Fig. 8, which was from a decalcified bone slice with high-grade osteosarcoma from the femur. The necrotic tumor (Supplementary Fig. 8b) and the viable tumor (Supplementary Fig. 8c-d) can be identified using the PAM images, which also showed comparable features as the H&E-stained images (Supplementary Fig. 8f-g).

Photoacoustic virtual histology via deep learning.

To match traditional histologic images, we performed virtual H&E staining on the grayscale PAM images using a CycleGAN based deep learning method[36]. The virtual staining CycleGAN network architecture is shown in Fig. 6. More detailed procedures of generating virtually H&E-stained PAM images are described in Methods. The example UV-PAM images of the bone section are shown in grayscale contrast (Supplementary Fig. 9) and histology-like pseudocolor (Fig. 7a and Fig. 7c), which demonstrate architectural features as well as cellular details similar to the corresponding H&E images (Fig. 7b and Fig. 7d). The close-up virtual histologic PAM images (Fig. 7a1-a2 and Fig. 7c1-c2) clearly demonstrate histologic features that would be important in the interpretation of pathological examination and correspond to the close-up H&E images (Fig. 7b1-b2 and Fig. 7d1-d2). The virtual histologic images have been reviewed by three pathologists and one orthopedic surgeon, who confirmed the comparable and interpretable histologic features present in H&E-stained slides that might be used for clinical diagnosis. More details of close-up images from the virtually stained PAM images and corresponding H&E-stained images are shown in Supplementary Movie 2 and Supplementary Movie 3 for side-by-side comparison. The cell nuclear counts, nuclear cross-sectional areas, and internuclear nearest neighbor distances are quantitatively compared in Supplementary Fig. 10 and Supplementary Table. 2, demonstrating a good match between the virtual staining photoacoustic image and the corresponding real H&E-stained image. As shown in Supplementary Table. 2, internuclear distances in two images match within the errors. The cell counts and nuclear cross-sectional areas are slightly different, which is expected as we were looking at neighboring sections taken at different axial positions instead of the same section.

Discussion

The development of 3D contour-scanning UV-PAM in reflection mode enables more rapid pathological examination of bone specimens. In contrast, traditional pathological examination techniques for bone involve time-consuming decalcification procedures, and the frozen section technique is often not applicable. With the bone mineral as its major component, dense cortical bones can take days to decalcify before it is soft enough to be sectioned into thin slices, which prevents rapid intraoperative diagnosis. Currently, orthopedic surgeons heavily rely on pre-operative x-ray CT or MRI to identify the extent of the tumor for the planning of resection margins. But these imaging modalities cannot provide accurate diagnosis and intraoperative confirmation of tumor margins. The reflection-mode contour-scanning UV-PAM enables label-free imaging of unprocessed thick bone samples with rough surfaces, which provides detailed information for pathological examination of the tumor margin rapidly, meeting a critical need for intraoperative margin analysis.

When rendering a diagnosis from standard H&E-stained slides, pathologists examine the architecture morphology and cellular features such as cell nuclei, cytoplasm, and extracellular matrix. The H&E staining approach has been long and widely used in histology, as it provides a clear contrast between cell nuclei and cytoplasmic parts by staining them in different colors. Thus, pathologists are accustomed to the stained and

counterstained appearance of H&E-stained tissue samples, which show extracellular matrix and cytoplasm as pink, and cell nuclei as blue/purple. At the UV wavelength of 266 nm[38], the cell nuclei have a much higher absorption coefficient and PA amplitudes than the extracellular matrix and cytoplasm, allowing the virtual labeling of them in different colors like H&E staining. We processed the grayscale PAM images and generated the pseudocolor images for virtual H&E staining by applying the deep learning approach with CycleGAN, which does not need well-aligned PAM and H&E-stained image pairs for neural network training. The virtually stained pseudocolor PAM images demonstrated cellular, nuclear, and cytoplasmic detail, matching the corresponding H&E-stained images. With more clinically relevant PAM virtual histology results, the deep convolutional neural network technique may be further used to potentially achieve automatic diagnosis and tumor margin detection[16].

Although we have demonstrated the potential of UV-PAM for rapid diagnosis of unprocessed bone specimens, further improvements can be made toward better clinical use. One key challenge is to improve the image speed to allow for faster feedback intraoperatively. The current UV-PAM system employs a pulsed 266 nm laser with a pulse repetition rate up to 50 kHz, which limited the theoretical image speed to an A-line rate of 50 kHz. However, due to the accuracy and stability of step motors, it is challenging to ensure a good image quality of UV-PAM at high motor speeds. The current system is running at 10 kHz laser repetition rate, which takes about 10 minutes in practice to scan a FOV of 1x1 mm^2 at the step size of 0.625 μm. To achieve higher imaging speeds, we can use faster optical scanning approaches and even higher laser repetition rates[39]. Moreover, multichannel parallel imaging can be used to further boost the imaging speed, where multiple focal spots and an ultrasound transducer array are used for image reconstruction. For instance, a microlens array can be utilized to create multiple focal spots for multichannel parallel imaging, which has been reported to improve the imaging speed of UV-PAM by 40 times[40]. However, the limited numerical aperture and the short working distance of the microlens array can only be used in transmission-mode UV-PAM, which impedes its practical use for high-resolution images of thick unprocessed biological samples. Reflection-mode multichannel UV-PAM with high resolution will be needed for faster intraoperative diagnosis.

Due to the physical limit of z-motor mechanical movement, which cannot adjust the position fast enough, a small portion (e.g., ~6.3% in Fig. 2c) of the areas may still fall out of the DOF if we scan a large FOV (e.g., 6x8 mm^2). To further improve the performance of high-resolution PAM imaging of rough surfaces, an electrically tunable lens (ETL) may be integrated into our system to allow faster optical focus shifting with high accuracy[41]. Since the acoustical DOF of the focused ultrasonic transducer is often much longer (i.e., hundreds of microns) than the optical DOF, the optical focus shifting within the acoustic DOF can be used to compensate for the steep height fluctuation, while the time-dependent gain compensation technique can be used to compensate for the transducer sensitivity difference within the acoustic DOF[42].

Compared with traditional intraoperative pathological methods (i.e., frozen sectioning), photoacoustic histology can lower the cost by reducing the turnaround time and avoiding highly specific personnel for sample preparation and specimen transportation. It may also

enable remote and automatic pathological diagnostics in the future. The current UV-PAM system employs a Q-switched Nd: YLF nanosecond pulsed UV laser at the wavelength of 266 nm to generate photoacoustic signals of cell nuclei, which may be challenging for *in vivo* imaging due to the safety concern of UV laser. The need for nanosecond pulsed UV laser increases the cost of the PAM system. Further developments using longer laser wavelengths for photoacoustic histological imaging will not only enable in vivo imaging but also significantly lower the equipment cost. Another limitation is that the current system requires specimens to be mounted onto a sample holder and immersed into water for mechanical scanning and acoustic coupling, which is suboptimal for high-throughput histological imaging. A better configuration that allows the specimen outside the water tank will ensure even easier sample handling for rapid high-throughput histological imaging.

In summary, we have demonstrated label-free UV-PAM as a valid way to image unprocessed bone without the need for tissue sectioning. The immediate clinical indication for these results is to provide the possibility of rapid pathological examination of bone tumor margins. Since no physical sectioning is needed, it does not need highly specific trained technicians for bone specimen preparation. Moreover, the undestructed bone specimen can be further examined by other techniques after label-free UV-PAM imaging. In this paper, we focused on the demonstration of bone, which is one of the most challenging biological tissues for rapid pathological diagnosis. But the system can also be applied to various other types of specimens. We believe it has great potential for revolutionizing the pathological diagnosis and providing immediate feedback for determining the tumor margin.

Methods

Label-free reflection-mode UV-PAM.

The reflection-mode UV-PAM system used an Nd: YLF (neodymium-doped yttrium lithium fluoride) Q-switched 266 nm nanosecond pulsed laser (QL266-010-O, CrystaLaser). A bandpass glass filter (FGUV5, Thorlabs) was placed at the laser output to reject the leaked pump light. After passing the colored glass filter, a small portion of the beam was reflected by a UV fused silica beam sampler (BSF10-UV, Thorlabs) and directed to a Si photodiode (PDA36A, Thorlabs) for pulse-to-pulse fluctuation compensation. The UV laser beam was expanded by a pair of plano-convex lenses and spatially filtered by a 15 μm high-energy pinhole (900PH-15, Newport). The expanded and collimated beam was then focused onto the sample by a custom-made water-immersion UV objective lens (consisting of an aspheric lens, a concave lens, and a convex lens (NT49-696, NT48-674, NT46-313, Edmund Optics)) with a numerical aperture (NA) of 0.16. A customized ring-shaped ultrasonic transducer (42 MHz center frequency, 76% −6 dB two-way bandwidth) with a central aperture was used to detect the PA signal, which allows the optical and acoustical confocal alignment. The detected signal was amplified by two low noise amplifiers (ZFL-500LN+, Mini-Circuits) and digitized by the data acquisition card (ATS 9350, Alazar Technologies) at a 500 MHz sampling rate. The PAM image was acquired by scanning the water-immersed sample mounted onto a customized 3D scanner (consisting of 3 step motors, PLS-85, PI Micos, GmbH). The reconfigurable I/O device (myRIO-1900, National Instruments) with a field-

programmable gate array (FPGA) was used to control and synchronize laser pulses, motor movements, and data acquisition.

Real-time 3D contour-scanning UV-PAM.

To allow imaging of the rough surface of unprocessed thick samples like bone, we developed the contour scanning mechanism without prior knowledge of the sample surface using a 3-axis motorized stage, which ensures consistent lateral resolution within a large field of view. For consistent and optimized optical resolution, the distance between the sample and optical focus should be maintained within the DOF during scanning. In contour scanning, the time-of-flight information of PA signals is used to calculate the distance between the sample and the focal spot, which can be adjusted by the z-motor during scanning. With the numerical aperture of 0.16, the DOF of our UV-PAM microscope is only about 9 μm, which corresponds to 6 ns ultrasound propagation for the speed of sound at 1500 m/s in room temperature water. The acquired PA signal was digitized at the sampling rate of 500 MHz (ATS9350, AlazarTech). The z-profile of the sample surface can be accurately calculated using the time-of-flight information of PA signals, enabling contour scanning for z-position compensation.

Prior to PAM imaging, the optical and acoustic foci are confocally aligned, while the propagation time of the acoustic signal from the optical focus is recorded to determine the focal spot position. To extract the ultrasound propagation time, we calculate the centers of positive and negative peak positions in PA A-line signals, which are converted to the sample position. Without prior knowledge of the sample surface profile, one seed B-scan with the z-motor disabled is implemented to calculate the starting contour trajectory. To avoid potential noise interference and remove outliers, a 100-point moving average is used to generate a smooth z scanning trajectory. During the contour scanning, both the x-axis motor and the z-axis motor move simultaneously. After the first contoured B-scan, the z-motor trajectory and the distance between the sample surface and the ultrasonic transducer are calculated and used to compute the accurate surface profile. Due to the small y step (0.625 μm), we set the second z-motor trajectory to follow the surface profile from the previous contoured B-scan[43]. Then, the surface profile is updated according to the second contoured B-scan. This process is repeated until the whole scanning is completed. Real-time data processing and system control are implemented using MATLAB and LabVIEW hybrid programming.

Bone specimen preparation and H&E imaging.

The bone specimens for UV-PAM imaging were procured from larger specimens in the pathology laboratory with informed consents of patients, surgically removed from patients at the City of Hope and UCLA medical center. All bone specimens were fixed in 10% buffered formalin prior to any other procedures. For thick undecalcified specimens in this study, the specimens were mounted to the sample holder for imaging without further processing. To decalcify specimens, we treated the bone specimens with a decalcifying solution containing chelating agents in dilute HCl, while the treatment time varied depending on the size and hardness of the specimens. After fixation and decalcification, the specimen was embedded in paraffin wax, sectioned into 5-micron thick slices, and placed on glass slides. Specimens

with less calcification were sectioned without decalcification. These slices were then processed with standard H&E staining and cover-slipped. The H&E-stained slides were imaged using either the standard optical microscope or the digital whole slide scanning (Leica Aperio AT2) with a 40X objective.

UV-PAM virtual histology via CycleGAN.

To reconstruct the UV-PAM images, we first calculated the PA amplitude of each A-line signal after the Hilbert transform. The pulse energy measured by the photodiode was used to normalize the PA amplitude and compensate for the laser pulse fluctuation. The axial position of the specimen surface was calculated by detecting the peak of the A-line signal after the Hilbert transform. The 2D MAP (maximal amplitude projection) image was self-normalized. Since the PA amplitude of the contrast is proportional to its absorption coefficient, it can be used to effectively differentiate cell nuclei, cytoplasm, and the background. The cell nuclei have the largest absorption coefficient at 266 nm and the highest PA signals. After calculating the grayscale UV-PAM, we use a trained neural network to perform virtual H&E staining, which is more familiar to pathologists and thus easier for them to interpret.

We use the CycleGAN architecture[36], shown in Fig. 6, which can learn how to map images from the UV-PAM domain, PA, to the H&E domain, HE, without the need for well-aligned image pairs. We use an adversarial loss to learn the transformations G: PA HE and F: HE PA, such that the images G(PA) and F(HE) are indistinguishable from HE and PA, respectively. The discriminators are trained to distinguish between real images and those produced by the generators. The loss function for D_{HE} is given by[44]

$$l^{D_{HE}} = D_{HE}(G(PA))^2 + (1 - D_{HE}(HE))^2,$$

(1)

where PA is a UV-PAM image patch, and HE is an H&E-stained image patch. Similarly, the loss function for D_{PA} is given by

$$l^{D_{PA}} = D_{PA}(F(HE))^2 + (1 - D_{PA}(PA))^2.$$

(2)

The generators are trained to try and fool the discriminators by producing images that match the statistical properties of the target domain. To ensure G doesn't simply produce convincing but irrelevant H&E images, an additional loss term is necessary. Conventionally, this would be the l_2 or l_1 norm loss between the network output and some known ground truth image. However, this requires well-aligned paired datasets, which are challenging to acquire after sample preparation.

Instead, the CycleGAN architecture learns the inverse transformation so that cycle consistency can be used to ensure the images are of the same structures. The total loss for the generators is

$$l^G = (1 - D_{HE}(G(PA)))^2 + (1 - D_{PA}(F(HE)))^2 + \lambda \mid F(G(PA)) - PA \mid + \lambda \mid G(F(HE)) - HE \mid,$$

(3)

where the regularization parameter λ is set to 10.

The generators are residual networks consisting of an input convolutional layer, two convolutional layer and downsampling blocks, nine residual network blocks, two convolutional and upsampling blocks, and finally, an output convolutional layer[45]. Instance normalization and rectified linear unit (ReLU) layers are used after each convolutional layer. For the discriminator, we use PatchGAN consisting of convolutional layer and downsampling blocks, which classify whether the image is real on overlapping 70x70 pixel image patches[46]. This patch size is a compromise between promoting high spatial frequency fidelity and avoiding tiling artifacts. In the discriminator networks, instance normalization and leaky ReLU (lReLU) layers, $lReLU(x) = \max(0.2x, x)$ are used after each convolutional layer. Anti-alias downsampling and upsampling layers are used in both the generators and discriminators to improve shift invariance[47].

The training dataset consisted of UV-PAM images of undecalcified bone specimens. These images were converted into 17940 and 26565 286x286 pixel image patches for UV-PAM and H&E histology, respectively. During training, these were further randomly cropped to 256x256 for data augmentation. The training was performed with the Adam solver with a batch size of 4 and an initial learning rate of 0.0002, decaying to zero over 100 epochs[48]. Once trained, we used the generator G to transform UV-PAM data in overlapping 256x256 pixel image patches, which were recombined with linear blending. To validate the virtual histology performance, we have quantitatively assessed the accuracy of our virtual staining method. We have segmented the cell nuclei in comparative regions of interest to compare their numbers, sizes, and densities. The nuclear segmentation was performed via Qupath[49], using the default cell detection settings with the threshold set to 0.3 to reduce false positives. The cell counts, average nuclear areas, and average nearest neighbor internuclear distances were calculated for comparison of the UV-PAM virtual histology and H&E results.

Supplementary Material

Refer to Web version on PubMed Central for supplementary material.

Acknowledgements

Data availability

The authors declare that all data supporting the findings of this study are available within the paper and its Supplementary Information. The training dataset and the fake output images for the CycleGAN network are available online (https://doi.org/10.5281/zenodo.6345772). Other raw data are too large to be publicly shared, yet they are available for research purposes from the corresponding authors on reasonable request.

Code availability

The original code for CycleGAN is available at https://github.com/junyanz/pytorch-CycleGAN-and-pix2pix. We applied this to our dataset with the customized settings described in Methods. MATLAB was used for creating image tiles for the network and restitching output image tiles. The quantitative analysis of photoacoustic virtual histology was done via QuPath (https://qupath.github.io/). The system control software and the data collection software are proprietary and used in licensed technologies.

References

1. World Health Organization Global Cancer Observatory. Available Online: http://gco.iarc.fr/today/home (accessed on May 19 2021).

2. Wyld L, Audisio RA & Poston GJ The evolution of cancer surgery and future perspectives. Nat Rev Clin Oncol 12, 115–124 (2015). [PubMed: 25384943]

3. Sullivan R et al. Global cancer surgery: delivering safe, affordable, and timely cancer surgery. The Lancet Oncology 16, 1193–1224 (2015). [PubMed: 26427363]

4. Mahe E et al. Intraoperative pathology consultation: error, cause and impact. Can J Surg 56, E13–E18 (2013). [PubMed: 23706852]

5. DiNardo LJ, Lin J, Karageorge LS & Powers CN Accuracy, utility, and cost of frozen section margins in head and neck cancer surgery. Laryngoscope 110, 1773–1776 (2000). [PubMed: 11037842]

6. Brender E, Burke A & Glass RM Frozen Section Biopsy. JAMA 294, 3200–3200 (2005). [PubMed: 16380598]

7. Campanacci M Bone and Soft Tissue Tumors: Clinical Features, Imaging, Pathology and Treatment. (Springer Science & Business Media, 2013).

8. Organization, W. H. & Cancer, I. A. for R. on. Pathology and Genetics of Tumours of Soft Tissue and Bone. (IARC, 2002).

9. Taqi SA, Sami SA, Sami LB & Zaki SA A review of artifacts in histopathology. J Oral Maxillofac Pathol 22, 279 (2018).

10. Gomez-Brouchet A et al. Assessment of resection margins in bone sarcoma treated by neoadjuvant chemotherapy: Literature review and guidelines of the bone group (GROUPOS) of the French sarcoma group and bone tumor study group (GSF-GETO/RESOS). Orthopaedics & Traumatology: Surgery & Research 105, 773–780 (2019).

11. Gareau DS et al. Confocal mosaicing microscopy in Mohs skin excisions: feasibility of rapid surgical pathology. J Biomed Opt 13, 054001 (2008). [PubMed: 19021381]

12. Wang M et al. Gigapixel surface imaging of radical prostatectomy specimens for comprehensive detection of cancer-positive surgical margins using structured illumination microscopy. Sci Rep 6, 27419 (2016). [PubMed: 27257084]

13. Wang M et al. High-Resolution Rapid Diagnostic Imaging of Whole Prostate Biopsies Using Video-Rate Fluorescence Structured Illumination Microscopy. Cancer Res 75, 4032–4041 (2015). [PubMed: 26282168]

14. Glaser AK et al. Light-sheet microscopy for slide-free non-destructive pathology of large clinical specimens. Nat Biomed Eng 1, 1–10 (2017).

15. Fereidouni F et al. Microscopy with ultraviolet surface excitation for rapid slide-free histology. Nat Biomed Eng 1, 957–966 (2017). [PubMed: 31015706]

16. Hollon TC et al. Near real-time intraoperative brain tumor diagnosis using stimulated Raman histology and deep neural networks. Nat Med 26, 52–58 (2020). [PubMed: 31907460]

17. Orringer DA et al. Rapid intraoperative histology of unprocessed surgical specimens via fibre-laser-based stimulated Raman scattering microscopy. Nat Biomed Eng 1, 1–13 (2017).

18. Assayag O et al. Large field, high resolution full-field optical coherence tomography: a pre-clinical study of human breast tissue and cancer assessment. Technol Cancer Res Treat 13, 455–468 (2014). [PubMed: 24000981]

19. Nguyen FT et al. Intraoperative Evaluation of Breast Tumor Margins with Optical Coherence Tomography. Cancer Res 69, 8790–8796 (2009). [PubMed: 19910294]

20. Fereidouni F, Tracy J & M.d RML MUSE microscopy for thick tissue imaging with extended depth of field (Conference Presentation). in Optical Biopsy XVI: Toward Real-Time Spectroscopic Imaging and Diagnosis vol. 10489 104890H (SPIE, 2018).

21. Gambichler T et al. Comparison of histometric data obtained by optical coherence tomography and routine histology. JBO 10, 044008 (2005).

22. Wang LV & Hu S Photoacoustic Tomography: In Vivo Imaging from Organelles to Organs. Science 335, 1458–1462 (2012). [PubMed: 22442475]

23. Wang LV & Yao J A practical guide to photoacoustic tomography in the life sciences. Nat Methods 13, 627–638 (2016). [PubMed: 27467726]

24. Danielli A et al. Label-free photoacoustic nanoscopy. JBO 19, 086006 (2014). [PubMed: 25104412]

25. Shi J, Tang Y & Yao J Advances in super-resolution photoacoustic imaging. Quant Imaging Med Surg 8, 724–732 (2018). [PubMed: 30306053]

26. Yao J, Wang L, Li C, Zhang C & Wang LV Photoimprint Photoacoustic Microscopy for Three-Dimensional Label-Free Subdiffraction Imaging. Phys. Rev. Lett 112, 014302 (2014). [PubMed: 24483902]

27. Yao J et al. High-speed label-free functional photoacoustic microscopy of mouse brain in action. Nat Methods 12, 407–410 (2015). [PubMed: 25822799]

28. Li L et al. Single-impulse panoramic photoacoustic computed tomography of small-animal whole-body dynamics at high spatiotemporal resolution. Nat Biomed Eng 1, 1–11 (2017).

29. Wong TTW et al. Fast label-free multilayered histology-like imaging of human breast cancer by photoacoustic microscopy. Science Advances 3, e1602168 (2017). [PubMed: 28560329]

30. Zhang C, Zhang YS, Yao D-K, Xia Y & Wang LV Label-free photoacoustic microscopy of cytochromes. J Biomed Opt 18, 020504 (2013). [PubMed: 23370407]

31. Xu Z, Li C & Wang LV Photoacoustic tomography of water in phantoms and tissue. J Biomed Opt 15, 036019 (2010). [PubMed: 20615021]

32. Wong TTW et al. Label-free automated three-dimensional imaging of whole organs by microtomy-assisted photoacoustic microscopy. Nat Commun 8, 1386 (2017). [PubMed: 29123109]

33. Shi J et al. High-resolution, high-contrast mid-infrared imaging of fresh biological samples with ultraviolet-localized photoacoustic microscopy. Nat. Photonics 13, 609–615 (2019). [PubMed: 31440304]

34. Tschuchnig ME, Oostingh GJ & Gadermayr M Generative Adversarial Networks in Digital Pathology: A Survey on Trends and Future Potential. Patterns 1, 100089 (2020). [PubMed: 33205132]

35. Rivenson Y et al. Virtual histological staining of unlabelled tissue-autofluorescence images via deep learning. Nat Biomed Eng 3, 466–477 (2019). [PubMed: 31142829]

36. Zhu J-Y, Park T, Isola P & Efros AA Unpaired Image-to-Image Translation using Cycle-Consistent Adversarial Networks. arXiv:1703.10593 [cs] (2020).

37. Lahiani A et al. Virtualization of tissue staining in digital pathology using an unsupervised deep learning approach. arXiv:1810.06415 [cs] (2018).

38. Yao D-K, Chen R, Maslov K, Zhou Q & Wang LV Optimal ultraviolet wavelength for in vivo photoacoustic imaging of cell nuclei. J Biomed Opt 17, 056004 (2012). [PubMed: 22612127]

39. Li X, Kang L, Zhang Y & Wong TTW High-speed label-free ultraviolet photoacoustic microscopy for histology-like imaging of unprocessed biological tissues. Opt. Lett., OL 45, 5401–5404 (2020).

40. Imai T et al. High-throughput ultraviolet photoacoustic microscopy with multifocal excitation. JBO 23, 036007 (2018). [PubMed: 29546734]

41. Li B, Qin H, Yang S & Xing D In vivo fast variable focus photoacoustic microscopy using an electrically tunable lens. Opt Express 22, 20130–20137 (2014). [PubMed: 25321222]

42. Tang M, Luo F & Liu D Automatic Time Gain Compensation in Ultrasound Imaging System. in 2009 3rd International Conference on Bioinformatics and Biomedical Engineering 1–4 (2009). doi:10.1109/ICBBE.2009.5162432.

43. Xu Z et al. Cortex-wide multiparametric photoacoustic microscopy based on real-time contour scanning. NPh 6, 035012 (2019).

44. Mao X et al. Least Squares Generative Adversarial Networks. arXiv:1611.04076 [cs] (2017).

45. He K, Zhang X, Ren S & Sun J Deep Residual Learning for Image Recognition. arXiv:1512.03385 [cs] (2015).

46. Isola P, Zhu J-Y, Zhou T & Efros AA Image-to-Image Translation with Conditional Adversarial Networks. arXiv:1611.07004 [cs] (2018).

47. Zhang R Making Convolutional Networks Shift-Invariant Again. arXiv:1904.11486 [cs] (2019).

48. Kingma DP & Ba J Adam: A Method for Stochastic Optimization. arXiv:1412.6980 [cs] (2017).

49. Humphries MP, Maxwell P & Salto-Tellez M QuPath: The global impact of an open source digital pathology system. Computational and Structural Biotechnology Journal 19, 852–859 (2021). [PubMed: 33598100]
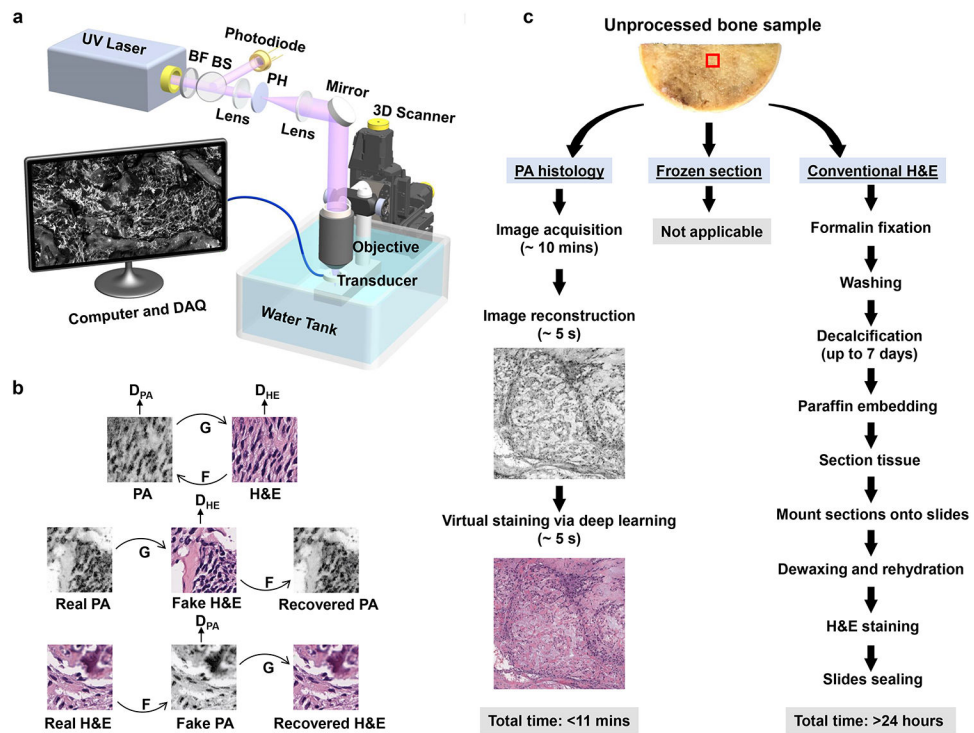
Fig. 1. Rapid label-free UV photoacoustic (PA) histology via deep learning.
a, schematic of the 3D contour scan UV-PAM system. The UV laser is spectrally filtered by a bandpass colored glass filter (BF) and spatially filtered and expanded using a pair of lenses and a pinhole (PH). The beam sampler (BS) is placed before the lens to pick up a small fraction of the beam for photodiode measurement to compensate for the laser pulse-to-pulse energy fluctuation. The collimated and expanded beam is focused through a ring-shaped ultrasound transducer using a customized water immersed objective and illuminates the specimen for photoacoustic excitation. The 3D contour scanning of the specimen placed on the sample holder is implemented for UV-PAM imaging. **b**, Deep learning network architecture for virtual staining of PAM images. The CycleGAN model consists of two generators, G: PA→H&E and F: H&E→PA, and corresponding adversarial discriminators, D_{PA} and D_{HE}. **c**, The workflow for PA histology and conventional H&E staining histology of bone samples (1x1 mm^2 field of view).
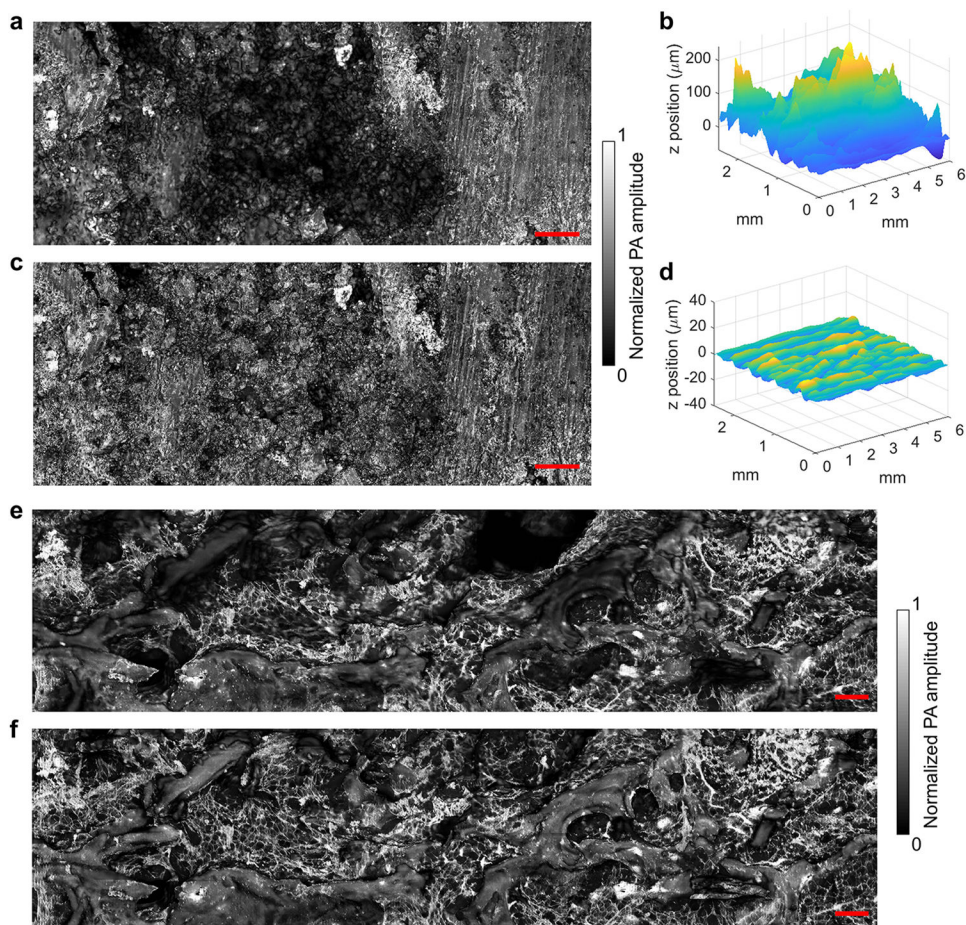
Fig. 2. Label-free 3D contour-scanning UV-PAM of thick (>1 cm) unprocessed bone specimens. a, The UV-PAM images of the undecalcified left tibia bone extracted from a patient with osteofibrous dysplasia-like adamantinoma acquired by **a** 2D raster-scanning and **c** 3D contour scanning, showing the improved image quality by 3D contour scanning of the undecalcified bone specimen with a rough surface. Scale bar, 500 μm. The specimen surface position in the axial direction relative to the optical focal plane during **b** 2D raster scanning and **d** 3D contour scanning profiles are calculated by the time-of-flight information of the photoacoustic signal. A normal unprocessed thick bone sample is also imaged and compared using **e** 2D raster scanning and **f** 3D contour scanning. Scale bar, 250 μm.
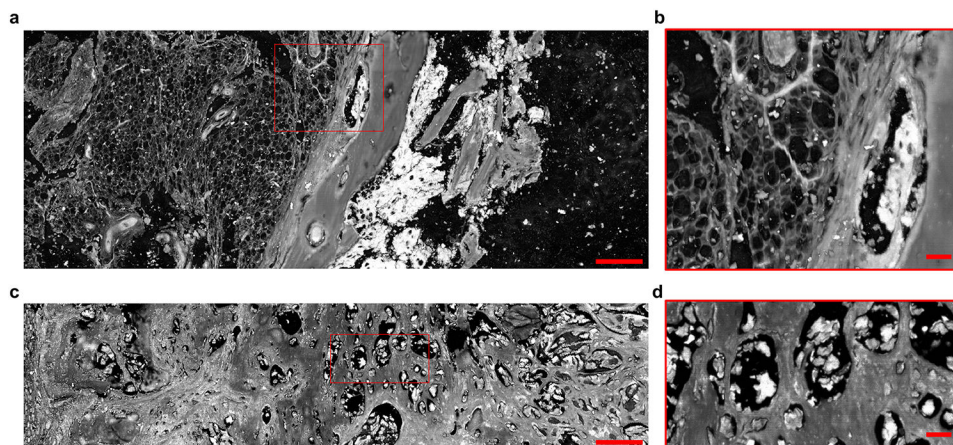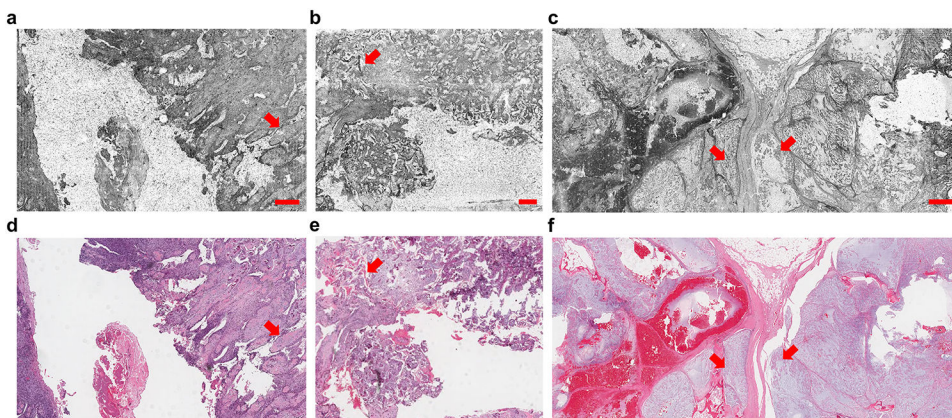
Fig. 3. Label-free UV-PAM of decalcified bone specimens.
a, PAM image of the formalin-fixed paraffin-embedded (FFPE) decalcified nonneoplastic bone fragment on a glass slide. A near vertically oriented trabecula of cancellous bone is seen in the middle portion of the image. Scale bar, 500 μm. **b,** A close-up image of **a** showing a portion of the cancellous bone at the left border of the image. Scale bar, 100 μm. **c,** PAM image of the FFPE decalcified bone specimen with metastatic poorly differentiated adenocarcinoma of pulmonary origin shows neoplastic glandular profiles of metastatic carcinoma on a glass slide. Scale bar, 500 μm. **d,** The close-up image of **c** shows nests and glandular profiles of metastatic carcinoma. Scale bar, 100 μm.
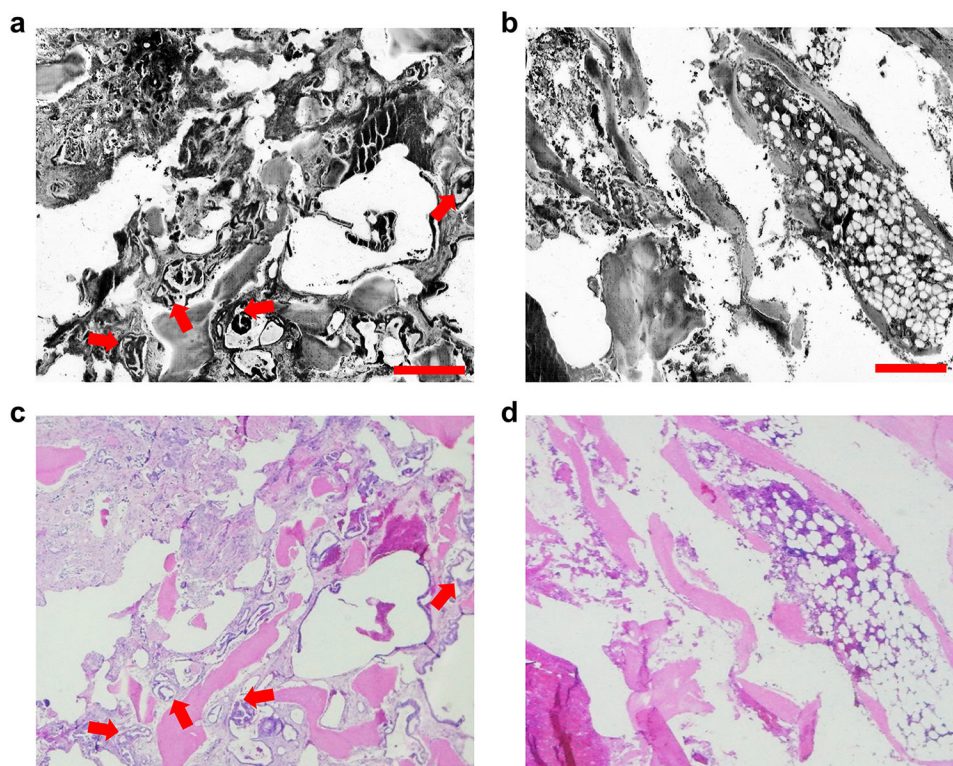
Fig. 4. Label-free UV-PAM for identifying tumors in decalcified bone fragments.
a, PAM image of the decalcified bone section on a glass slide with metastatic adenocarcinoma. **b,** PAM image of the decalcified bone section on a glass slide with normal bone fragment and hematopoietic marrow. The PAM contrast was reversed to highlight the high absorption region in dark color for better comparison. **c-d,** Corresponding H&E images of **a** and **b**. Neoplastic glands of metastatic carcinoma amongst bone fragments are indicated by arrows in **a** and **c**. Scale bars, 500 μm.
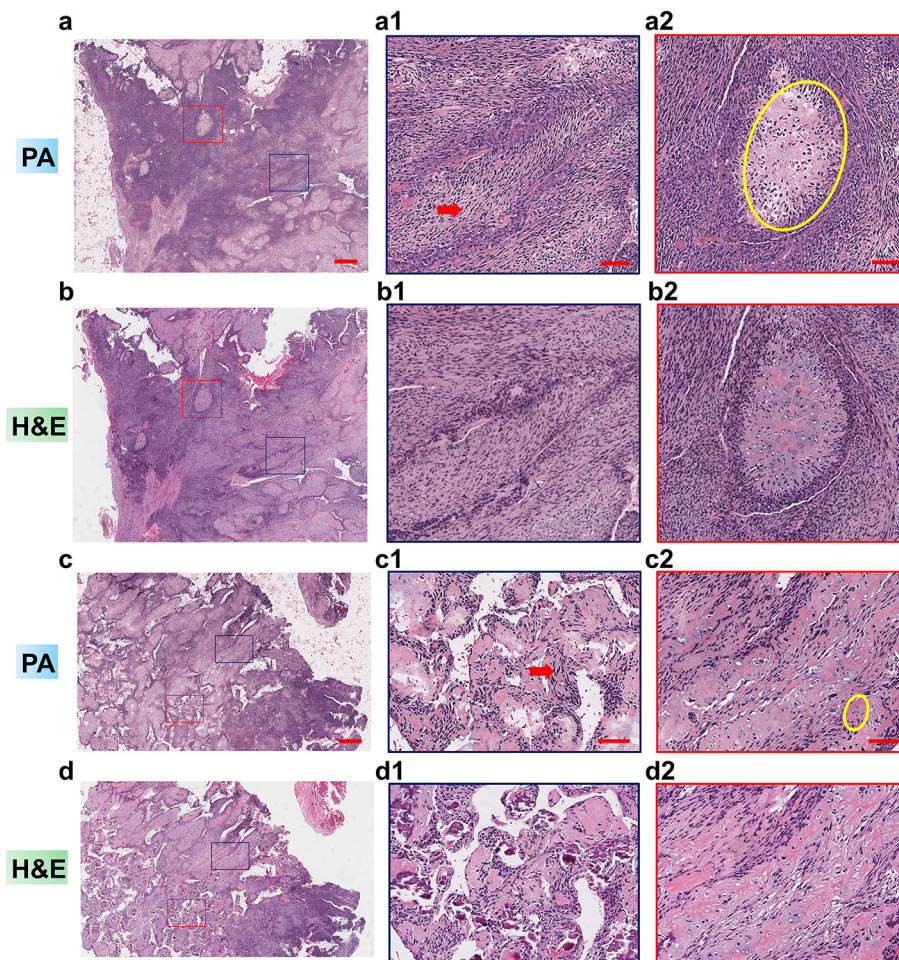
Fig. 5. Label-free UV-PAM of the undecalcified bone specimen and H&E validation.
a-b, UV-PAM images of undecalcified patient bone sections on a glass slide from patient #1 with osteoblastic osteosarcoma showing neoplastic osteoid matrix, the lacy material in between the nuclei of the neoplastic cells, denoted by arrows. **c,** UV-PAM images of an undecalcified patient bone section on a glass slide from patient #2 with chordoma, demonstrating lobules of the myxoid tumor demonstrating myxoid lobules of the tumor, which are areas denoted by arrows. **d-f,** Corresponding H&E images acquired by the digital whole slide scanning microscope with a 40X objective with an essentially identical appearance. Scale bars, 500 μm.
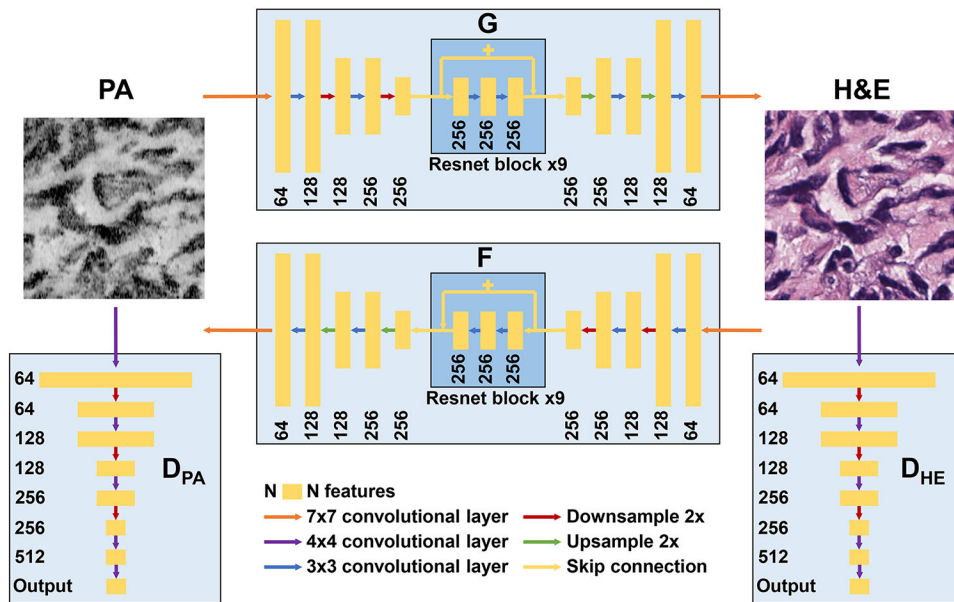
Fig. 6. Detailed network architecture for virtual staining.
The CycleGAN model consists of two generators, G: PA $\rightarrow$ HE and F: HE $\rightarrow$ PA, and corresponding adversarial discriminators, D_{PA} and D_{HE}. Each generator is composed of two downsampling blocks (a convolutional layer and anti-alias downsampling layer of stride two), nine residual blocks (two convolutional layers and a skip connection), and two upsampling blocks (an anti-alias upsampling layer of stride two and a convolutional layer). Each convolutional layer is followed by instance normalization and rectified linear unit (ReLU) activation layers. The discriminators are composed of three downsampling blocks, followed by an output convolutional layer. Each convolutional layer in the discriminators is followed by instance normalization and leaky ReLU activation layers. The network is applied to image patches of 256 by 256 pixels.

Fig. 7. Label-free UV-PAM virtual histology of undecalcified bone via unsupervised deep learning.

a, c, Virtual-stained PAM images of undecalcified bone sections on a glass slide. **b, d,** Corresponding H&E histology images. Scale bars, 500 μm. **a1-a2,** Close-up images of **a** show neoplastic spindle cells (denoted by many long, spindle-shaped purple nuclei, red arrow) arranged in vague streaming and fascicular patterns in **a1**, and a nodule of neoplastic chondroid material in **a2** (yellow circle), corresponding to the H&E-stained images in **b1** and **b2**. **c1-c2,** Close-up images of **c** show ribbons of neoplastic spindle cells (red arrow) in **c1** and disorganized osteoid, the streaky bands denoted by the yellow circle in **c2**, corresponding to the H&E-stained images in **d1** and **d2**. Scale bars, 100 μm.